Supporting Information for

Electronic structure of a graphene-like artificial crystal of $NdNiO_3$

Arian Arab[1], Xiaoran Liu[2], Okan Köksal[3], Weibing Yang[1], Ravini U. Chandrasena[1], Srimanta Middey[4], Mikhail Kareev[2], Siddharth Kumar[4], Marius-Adrian Husanu[5, 6], Zhenzhong Yang[7], Lin Gu[7, 8], Vladimir N. Strocov[5], Tien-Lin Lee[9], Jan Minár[10], Rossitza Pentcheva[3], Jak Chakhalian[2], and Alexander X. Gray[1,*]

[1] *Physics Department, Temple University, Philadelphia, Pennsylvania 19122, USA*

[2] *Department of Physics and Astronomy, Rutgers University, Piscataway, New Jersey 08854, USA*

[3] *Department of Physics and Center for Nanointegration Duisburg-Essen (CENIDE), University of Duisburg-Essen, Duisburg 47057, Germany*

[4] *Department of Physics, Indian Institute of Science, Bengaluru 560 012, India*

[5] *Swiss Light Source, Paul Scherrer Institute, 5232 Villigen, Switzerland*

[6] *National Institute of Materials Physics, 077125 Atomistilor 405A, Magurele, Romania*

[7] *Beijing National Laboratory for Condensed-Matter Physics and Institute of Physics, Chinese Academy of Sciences, Beijing 100190, People's Republic of China*

[8] *Collaborative Innovation Center of Quantum Matter, Beijing 100190, People's Republic of China*

[9] *Diamond Light Source Ltd., Didcot, Oxfordshire OX11 0DE, United Kingdom*

[10] *New Technologies-Research Center, University of West Bohemia, CZ-30614 Pilsen, Czech Republic*

**email: axgray@temple.edu*

METHODS

Sample Synthesis and Characterization. [2 u.c. $NdNiO_3$ / 4 u.c. $LaAlO_3$] ×3 superlattice was grown on $LaAlO_3$ (111) in layer-by-layer manner using a pulsed laser interval deposition system, equipped with high-pressure RHEED.[1,2] The growth was carried out at 670°C under 150 mTorr partial pressure of oxygen. The sample was annealed at the growth temperature for 30 minutes under 1 bar pressure of ultra-pure oxygen. The STEM measurements shown in Fig. S2 were carried out using a spherical aberration-corrected JEM-ARM200F microscope operated at 200 kV in the high-angle annular dark field (HAADF) imaging mode. The flat morphology of the surface was verified using AFM (see Fig. S3), revealing RMS roughness of approximately 200 pm (less than one unit cell). Crystallinity and correct layering of the superlattice was confirmed using high-resolution synchrotron-based x-ray diffraction (XRD) spectroscopy (see Fig. S4). In addition to this, an exhaustive characterization of this and similar [111] superlattices via in-situ RHEED, STEM, XRD, XAS, and AFM was carried out by us in prior studies, confirming crystallinity, layering, phase purity, coherence, morphology and relevant chemical/valence states of the constituent cations.[1,2,3]

Bulk-Sensitive Photoemission Spectroscopy. The SX-ARPES endstation at the high-resolution ADRESS beamline at the Swiss Light Source was equipped with a SPECS PHOIBOS-150 hemispherical electrostatic analyzer and a six-axis cryogenic manipulator, allowing for facile three-dimensional mapping of the valence-band electronic structure in the momentum space (k_x, k_y and k_z via variable photon energy). At the photon energy of 642 eV, total instrumental energy resolution was estimated to be 111 meV. The HAXPES measurements were carried out at Beamline I09 of the Diamond Light Source at the photon energy of 6.45 keV and with a comparable total experimental energy resolution of approximately 200 meV. It is important to note that due to the much higher photon energies utilized in SX-ARPES and HAXPES, the effective exprimental resolutions in both energy and momentum are limited, as compared to conventional high-resolution ARPES (~1-5 meV). Our

measurements represent the current status of the state-of-the-art for both SX-ARPES[4,5] and HAXPES.[6] Significant efforts in the instrumentation improvements of both the x-ray sources (beamlines/monochromators) and the photoelectron detectors (analyzers) are currently underway at several facilities, indicating that resolutions of <50 meV (for HAXPES) and <30-40 meV (for SX-ARPES) are achievable in the near future.

All the measurements were carried in the near-normal emission (NE) [111] experimental geometry. For the angle-resolved SX-ARPES measurements, the fixed angle of 70° between the beamline and the analyzer direction thus required the grazing incidence angle to be set at 20° (= 90° - 70°). The sample temperature was set to 100K.

Theoretical Calculations. Density functional theory (DFT+*U*) calculations were carried out with the all-electron full potential linearized augmented plane wave method in the WIEN2k code.[7,8] The generalized gradient approximation[9] was used for the exchange-correlation functional together with an on-site Hubbard *U* term[10] with *U* = 5.0 eV and J = 1.7 eV for Ni 3*d* and *U* = 8 eV for Nd. The 1×1 unit cell with P1 symmetry was modelled with a 30 atom supercell with the lateral lattice constant of $LaAlO_3$, while the $\sqrt{3}\times\sqrt{3}R30°$ reconstruction required a three-times-larger unit cell. Octahedral tilts and distortions were fully taken into account. The Fermi surface calculations for different isoenergetic levels were carried out with a very dense 30×30×10 *k*-point grid and plotted using the XCRYSDEN package.[11]

The SX-ARPES calculations were carried out within the framework of the fully-relativistic one-step model of photoemission,[12] as implemented in the multiple scattering Green function SPR-KKR package.[13] This method accounts for all relevant experimental aspects of the photoemission process, including experimental geometry, photon energies, x-ray polarization, matrix element effects, multiple scattering in the initial and final states, and all surface- and interface-related effects in the excitation process.

Figure S1

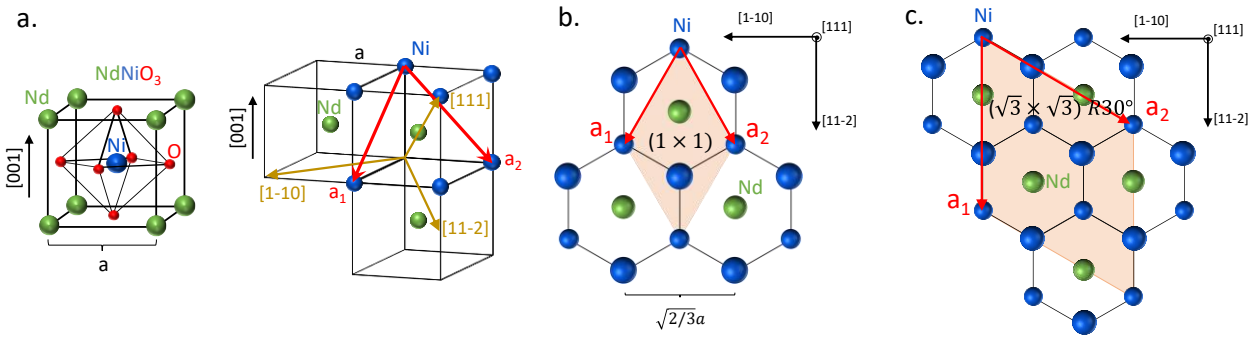

Figure S1. Structural diagram depicting the perovskite structure along the conventional [001] direction (a), and the difference between the P1 (1×1) and P3 (√3×√3) symmetries (b and c). For clarity, the structure is depicted in the pseudocubic notation (a) and the oxygen atoms are not shown (b and c). The diagram defines the sizes of the corresponding unit cells. The differences in orbital orientation of the Ni1 and Ni2 3*d* orbitals which lead to the larger unit cell of the P3 (√3×√3) symmetry are shown in Fig. 4 of Ref. 24 of the main text.

Figure S2

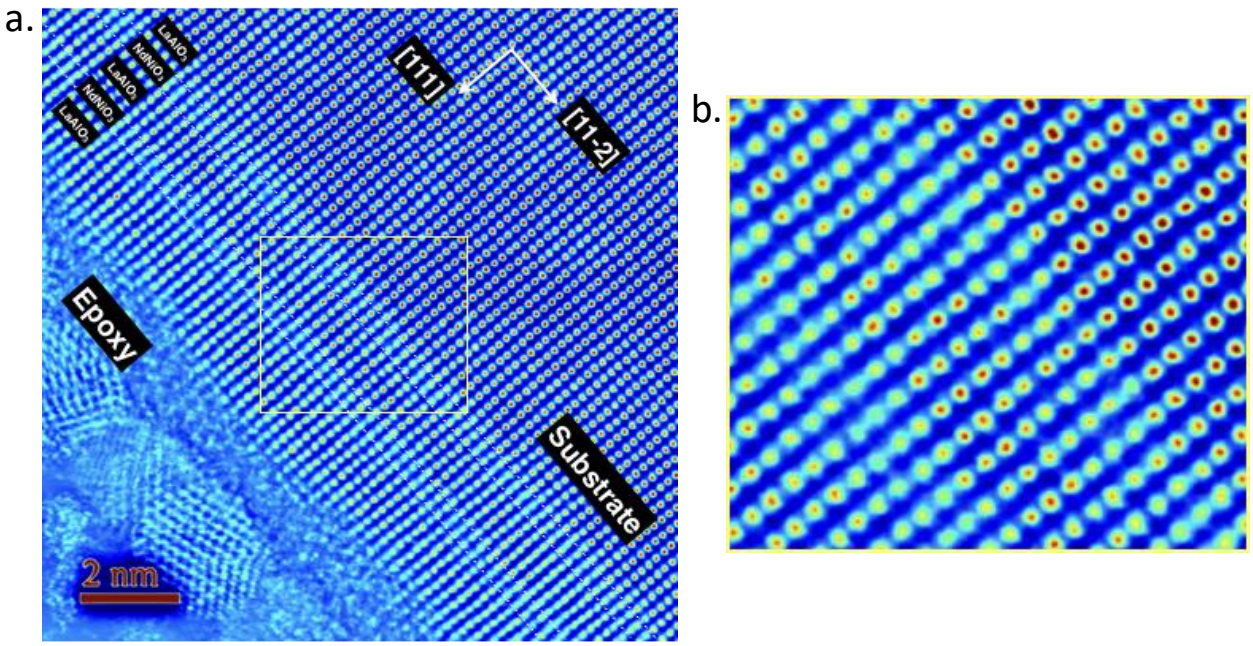

Figure S2. High-resolution STEM-HAADF cross-sectional image recorded along the [11-2] and [111] pseudocubic directions. (a) Large field-of-view (FOV) scan, spanning over 60 u.c. along the [11-2] (lateral) direction and showing continuous and coherent superlattice layering. (b) Magnified view of the area outlined by a yellow box in (a), showing two repetitions of the (111)-oriented [2 u.c. $NdNiO_3$ / 4 u.c. $LaAlO_3$] superstructure. We note that the ion-milling process used for STEM sample preparation damages several layers at the top surface, leading to partial imaging of the third supercell. The same sample as in Ref. [1] was imaged, but with a larger FOV and optimized post-processing. The color scale corresponds to the gray values of the pixels.

Figure S3

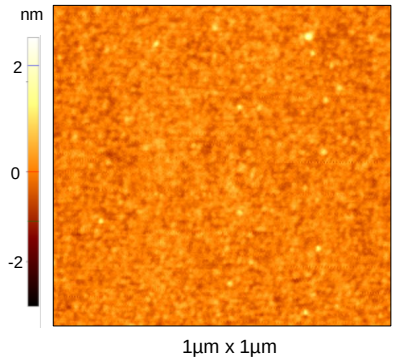

Figure S3. Atomic force microscopy (AFM) measurements of the [2 u.c. $NdNiO_3$ / 4 u.c. $LaAlO_3$] (111) superlattice grown on an $LaAlO_3$ (111) substrate. The RMS surface roughness was found to be approximately 200 pm (less than one unit cell), which confirms smooth surface morphology of the structure.

Figure S4

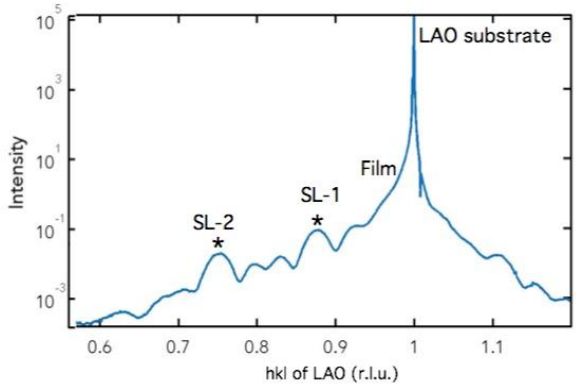

Figure S4. High-resolution synchrotron-based XRD spectroscopy measurements confirm growth along the [111] direction and exhibit thickness fringes as well as superlattice reflections (marked by *), as expected for a 2NNO/4LAO repeat unit (6 unit cells). The results suggest correct layering as well as atomically sharp interfaces and absence of chemical disorder over a macroscopically-large length scale.

Figure S5

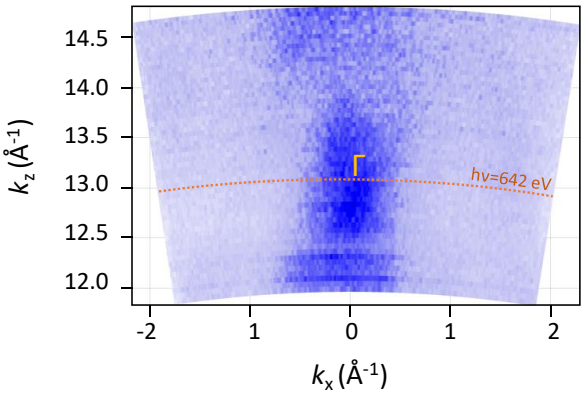

Figure S5. Momentum-resolved k_x-k_z map obtained by scanning the excitation x-ray photon energy. At the photon energy of 642 eV, the final photoelectron wave vector k_f points close to a high-symmetry point along the k_z direction in the extended BZ picture. It is important to note that in an ultrathin sample, spatial confinement of the initial state will introduce an intrinsic broadening in k_z, which will be equal to 1/(length of 3 supercells). However, in this case, such initial-state broadening is approximately three times smaller as compared to the final-state broadening, which is defined by 1/(photoelectron mean-free path at 642 eV). Thus, confinement effects could be considered negligible compared to the effects of the photoelectron mean-free path.[14]

Figure S6

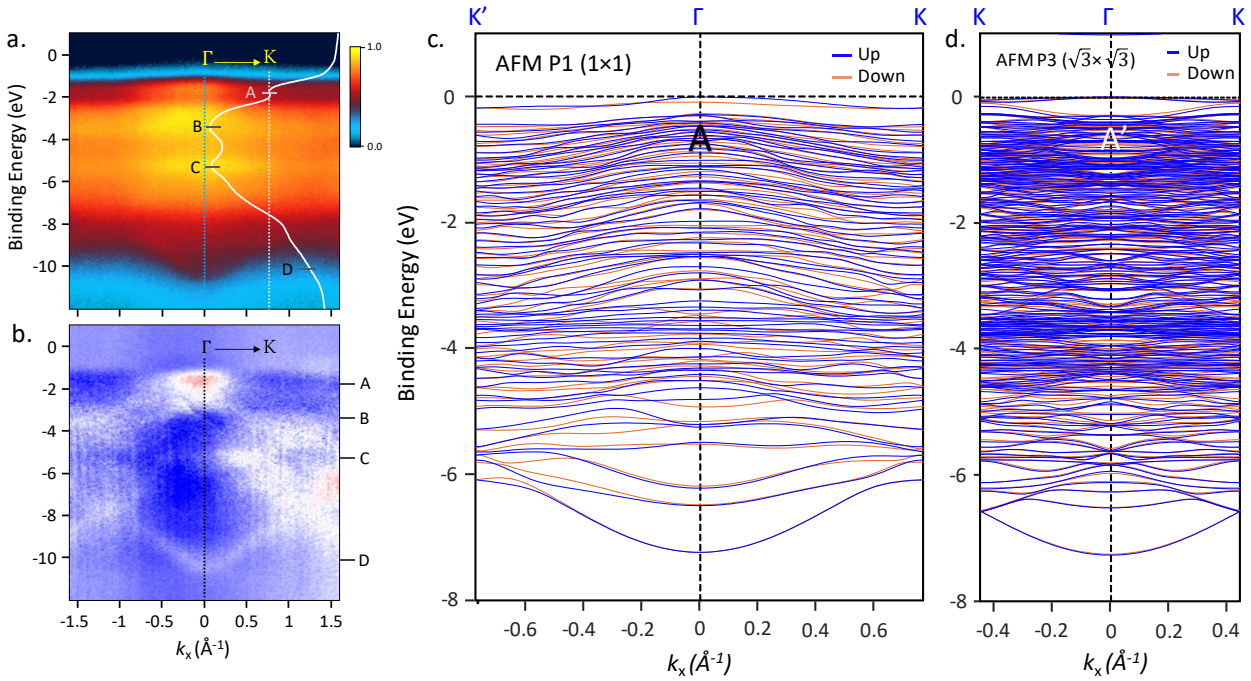

Figure S6. Comparison of the experimental data (a and b) and the band structure calculations for the P1 (1×1) and P3 (√3×√3) symmetries (c and d). In panel b, the raw spectrum was normalized by the binding-energy-averaged and the *k*-averaged spectra to enhance the dispersive features (*e.g.* A and D), while suppressing the non-dispersive features (*e.g.* B and C).

Discussion

One of the differences allowing to discriminate between the P1 (1×1) and P3 (√3×√3) symmetries is observed in the dispersion of the near-E_F bands labelled 'feature A', comprised mainly of the strongly-hybridized Ni 3*d* and O 2*p* states. In the raw experimental data (a), as well as in the normalized data (b), it is evident that the valence-band maximum for this feature occurs at the Γ point, where the bands get closer to the Fermi level. This is also seen in Fig. 3a of the main text, where the maximum intensity at the binding energy of feature A is observed at the center of the BZ (Γ point) and not at the K points. This is consistent with the behavior of the corresponding bands for the P1 (1×1) symmetry shown in c. Conversely, corresponding feature A' for the P3 (√3×√3) symmetry exhibits the opposite behavior – the bands have their maxima at the K points and a characteristic 'dip' near the Γ point (see panel d above), which is inconsistent with the experiment.

Another major quantitative difference between the two symmetries arises from the size of the BZ, which is √3 smaller for the P3 (√3×√3) symmetry (due to a larger unit cell). This difference becomes apparent by comparing the horizontal k_x scales in the figures above. A much better

quantitative agreement between the experiment and the P1 (1×1) symmetry is particularly obvious when comparing the width (along the k_x scale) and the curvature of the parabolic band labeled 'feature D' at the valence-band bottom (see panels b and c). If P3 ($\sqrt{3}\times\sqrt{3}$) was the case, the parabolic band would be noticeably 'compressed' and would be repeated several times within the experimental detector range (spanning several BZs) due to the smaller BZ size, which is inconsistent with the experiment.

The correct size and periodicity of the P1 (1×1) Brillouin zones in the extended BZ picture is evident in Fig. 3a of the main text, wherein the calculated schematic map of the extended BZ picture zone boundaries is overlayed on the experimental data, matching the hexagonal symmetry of the observed photoemission intensity distribution.

Figure S7

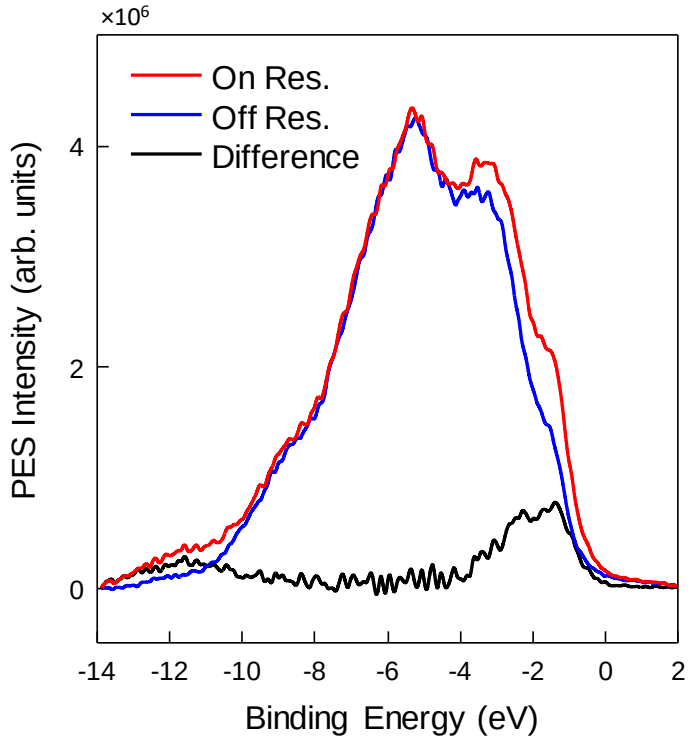

Figure S7. Extended-binding-energy range resonant photoemission data. Angle-integrated VB spectra recorded at the photon energies of 868.5 eV (off resonance) and 873.4 eV (on resonance) reveal the contribution of the Ni 3*d* states via resonant enhancement (see the black "difference" spectrum obtained by subtracting the 'off' spectrum from the 'on' spectrum.

Figure S8

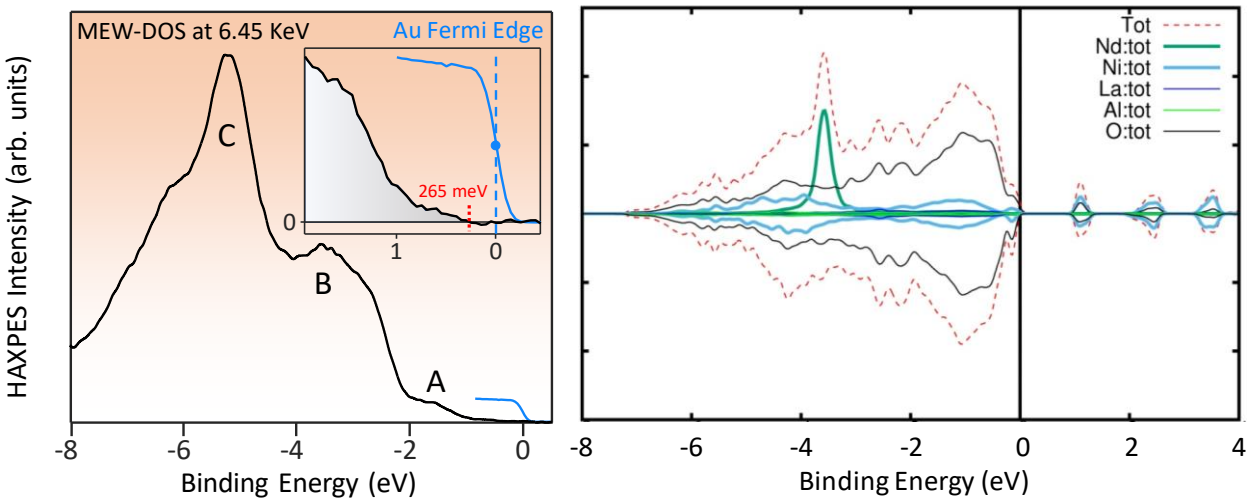

Figure S8. Comparison of the HAXPES measurement of the valence bands (left panel) and the theoretical DOS calculations (right panel), suggests that most of the 1.023 eV-wide full bandgap predicted by theory resides above the Fermi level. Measurement of the energy region below the Fermi level yields the value of the valence-band bandgap ($E_{\text{VB-max}} - E_{\text{F}}$) of 265 meV, qualitatively consistent with the theoretical picture shown in the right panel.

Figure S9

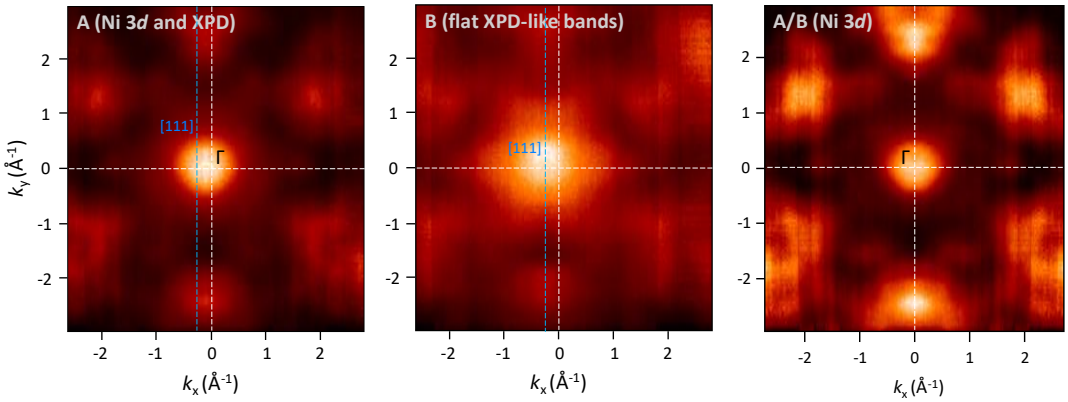

Figure S9. Separating band-dispersions in SX-ARPES from residual x-ray photoelectron diffraction (XPD). **a.** Non-normalized momentum-resolved photoemission intensity map of the VB feature A, containing combined contributions from the Ni 3*d* dispersive states and the XPD intensity modulations. The central intensity peak appears shifted toward the [111] emission direction due to a significant XPD contribution to the spectrum. **b.** Non-normalized photoemission intensity map of the VB feature B, comprised of flat XPD-like bands. The central intensity peak appears exactly along the [111] emission direction, confirming an overwhelming fraction of the XPD-derived intensity in the spectrum. **c.** XPD-corrected momentum-resolved photoemission intensity map of the VB feature A, obtained by scaled normalization A by B. Removal of the XPD effect shifts the central feature toward (0 Å^{-1},0 Å^{-1}), corresponding to the Γ-point in the first BZ.

Figure S10

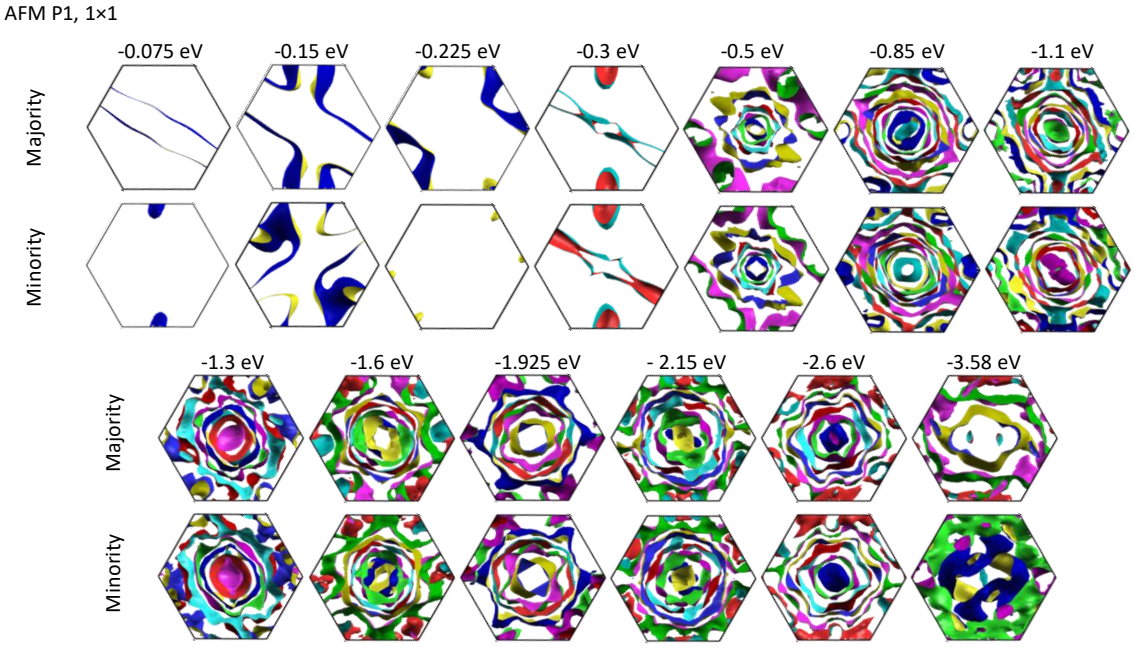

Figure S10. Isoenergetic cuts through the band structure in reciprocal space for the majority (top row) and minority (bottom row) bands, calculated for the binding-energy range from -0.075 eV to -3.58 eV, and spanning the major Ni 3*d* features in the VB manifold.

Figure S11

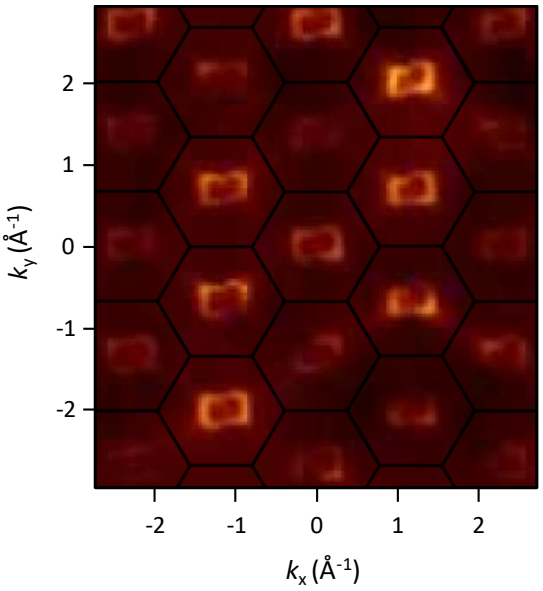

Figure S11. One step theory calculation of the momentum-resolved SX-ARPES spectra showing Ni 3*d* states near the Fermi level. Calculations were carried out using experimental SX-ARPES geometry for the photon energy of 642 eV. Clear modulations of the intensities between adjacent BZs due to the strong matrix-element effects are observed, consistent with the experimental observations.

References

[1] Middey, S.; Meyers, D.; Doennig, D.; Karrev, M.; Liu, X.; Cao, Y.; Yang. Z.; Shi, J.; Gu, L.; Ryan, P.J.; Pentcheva, R.; Freeland, J.W.; Chakhalian, J. Mott Electrons in an Artificial Graphenelike Crystal of Rare-Earth Nickelate. *Phys. Rev. Lett.* **2016**, 116, 056801.

[2] Middey, S.; Rivero, P.; Meyers, D.; Kareev, M.; Liu, X.; Cao, Y.; Freeland, J. W.; Barraza-Lopez S.; Chakhalian. J. Polarity compensation in ultra-thin films of complex oxides: The case of a perovskite nickelate. *Sci. Rep.* **2014**, 4, 6819.

[3] Middey, S.; Meyers, D.; Kareev, M.; Moon, E. J.; Gray, B. A.; Liu, X.; Freeland, J. W.; Chakhalian, J. Epitaxial growth of (111)-oriented $LaAlO_3/LaNiO_3$ ultra-thin superlattices. *Appl. Phys. Lett.* **2012**, 101, 261602.

[4] Horio, M.; Hauser, K.; Sassa, Y.; Mingazheva, Z.; Sutter, D.; Kramer, K.; Cook, A.; Nocerino, E.; Forslund, O. K.; Tjernberg, O.; Kobayashi, M.; Chikina, A.; Schroter, N. B. M.; Krieger, J. A.; Schmitt, T.; Strocov, V. N.; Pyon, S.; Takayana, T.; Takagi, H.; Lipscombe, O. J.; Hayden, S. M.; Ishikado, M.; Eisaki, H.; Neupert, T.; Mansson, M.; Matt, C. E.; Chang, J. Three-Dimensional Fermi Surface of Overdoped La-Based Cuprates. *Phys. Rev. Lett.* **2018**, 121, 077004.

[5] Weber, F.; Hott, R.; Heid, R.; Lev, L. L.; Caputo, M.; Schmitt, T.; Strocov, V. N. Three-dimensional Fermi surface of 2*H*−$NbSe_2$: Implications for the mechanism of charge density waves. *Phys. Rev. B* **2018**, 97, 235122.

[6] Woicik, J. C., ed. Hard X-ray Photoelectron Spectroscopy (HAXPES), **2016**, Vol. 59, Springer, Berlin, Germany.

[7] Schwarz, K.; Blaha, P. Solid state calculations using WIEN2k. *Computer. Matter. Sci.* **2003**, 28, 259-273.

[8] Blaha, P.; Schwarz, K.; Madsen, G. K. H.; Kvasnicka, D.; Luitz, J. Wien2k, An Augmented Plane Wave Plus Local Orbitals Program for Calculating Crystal Properties, ISBN 3-9501031-1-2 (Vienna University of Technology, Vienna, Austria, 2001).

[9] Perdew, J. P.; Burke, K.; Enzerhof, M. Generalized Gradient Approximation Made Simple. *Phys. Rev. Lett.* **1996**, 77**,** 3865-3868.

[10] Anisimov, V.I.; Zaanen, J.; Andersen, O.K. Band theory and Mott insulators: Hubbard *U* instead of Stoner *I*. *Phys. Rev. B.* **1991**, 44, 943-954.

[11] Kokalj, A. Computer graphics and graphical user interfaces as tools in simulations of matter at the atomic scale. *Computer. Matter. Sci.* **2003**, 28, 155-168.

[12] Braun, J.; Minar, J.; Ebert, H. Correlation, temperature and disorder: Recent developments in the one-step description of angle-resolved photoemission. *Phys. Rep.* **2018**, 740, 1-34.

[13] Ebert, H.; Ködderitzsch, D.; Minár, J. Calculating condensed matter properties using the KKR-Green's function method—recent developments and applications. *Rep. Prog. Phys.* **2011**, 74, 096501.

[14] Strocov, V. N. Photoemission response of 2D electron states. *J. Electron Spectrosc. Relat. Phenom.* **2018**, 229, 100-107.